Journal Name

ARTICLE TYPE

Cite this: DOI: 00.0000/xxxxxxxxxx

Stereoisomer-dependent unimolecular kinetics of 2,4-dimethyloxetane peroxy radicals

Anna C. Doner,[a] Judit Zádor,[b] and Brandon Rotavera[a,c*]

Received Date
Accepted Date

DOI: 00.0000/xxxxxxxxxx

2,4,dimethyloxetane is an important cyclic ether intermediate in low-temperature combustion systems. We determined the pressure- and temperature-dependent kinetics of seven cyclic ether peroxy radicals, which stem from 2,4,dimethyloxetane via H abstraction and O_2 addition. We used an automated kinetic workflow code, KinBot to tackle the complexity of the chemistry in a stereochemically resolved manner and solved the resulting master equations. We found that diastereomeric cyclic ether peroxy radicals have very different reactivities. Stereochemistry of the peroxy radical determines which QOOH isomerization steps are possible. Conventional QOOH decomposition pathways, such as cyclic ether formation and HO_2 elimination, compete with ring-opening reactions, which primarily produce OH radicals, and the outcome is very sensitive to the stereochemistry. Ring opening reactions lead to products, such as unsaturated, acyclic peroxy radicals, that form connections with other chemical kinetics mechanisms. These connections may complicate the interpretation of experimental results in the field.

1 Introduction

Low-temperature autooxidation of organic molecules follows a degenerate chain-branching mechanism that is driven by the formation of peroxy radicals (ROO) and their subsequent isomerization reactions into hydroperoxy-substituted carbon-centered radicals, QOOH.[1] Chain branching results from ensuing reactions of QOOH with O_2 in competition with its unimolecular reactions; the balance of the two types of reactions governs overall rates of oxidation. The unimolecular reactions of QOOH radicals can form conjugate alkene + HO_2 products, or cyclic ethers or other intermediates which are coincident with OH. The HO_2 forming pathways are chain inhibiting, while the OH forming ones are chain propagating. Autoignition properties are thus highly sensitive to the balance of these two kinds of pathways, and in turn the product yields are highly sensitive to the molecular structure of QOOH radicals. Experimental and theoretical investigations of these reactions are complicated, because they happen over complex, multi-well potential energy surfaces (PESs) that require a detailed master equation (ME) treatment to capture the underlying reactions' pressure and temperature dependence.

While QOOH radicals are central to low-temperature oxidation, they are very hard to detect in experiments, because they exist at very low steady state concentrations even in carefully prepared experiments on model systems.[2–5] As direct and unique products of QOOH radicals, cyclic ethers can provide a means of inferring reactions of QOOH radicals in low-temperature combustion, especially if they can be traced back to specific QOOH radicals based on their structure, e.g., their ring size. Cyclic ethers are also relevant in tropospheric reactions[6,7] and may form via epoxidation[8,9] or from reactions of alkoxy radicals.[10] Photolytically induced isomerization of organic peroxy radicals into QOOH[11] may provide an additional source of cyclic ethers in the troposphere.

Combustion mechanisms rely extensively on steady state concentration measurements of relatively stable species from flow reactor experiments. While the formation of cyclic ethers is included in models often in the form of rate rules,[12–16] there is an absence of rigorous sub-mechanisms for the further reactions of cyclic ethers. This is largely due to the lack of rigorous information about the consumption reactions, which include site-specific H-abstraction reactions, ring-opening of cyclic ether radicals, and reactions of cyclic

---

[*] *Corresponding author; E-mail: rotavera@uga.edu*

[a] *College of Engineering and* [c] *Department of Chemistry, University of Georgia, Athens, Georgia 30602, United States.*

[b] *Combustion Research Facility, Sandia National Laboratories, 7011 East Avenue, Livermore, CA 94550, USA.*

† Electronic Supplementary Information (ESI) available: The master equation input files containing all molecular properties; the master equation output containing the calculated rate coefficients and a related species dictionary with SMILES; potential energy surfaces organized by radicals; reaction pathways with chemical structures; examples of explored but excluded pathways; list of species with high T1 diagnostic. See DOI: 00.0000/00000000.

ether radicals with O_2. The latter can traverse QOOH-mediated pathways[17–19] in a manner similar to hydrocarbons but can have more complicated chemical behavior as well due to the heterocycle. It has been shown before that unimolecular reaction of cyclic ether peroxy radicals can lead to ketohydroperoxide-type radicals[17,18] and dicarbonyls.[18,20,21] For dicarbonyls, the typical formation pathway in chemical mechanisms is via ketohydroperoxide decomposition. Contributions via alternative pathways, such as cyclic ether oxidation may render unreliable the use of dicarbonyls as an experimental marker for ketohydroperoxide production – unless the cyclic ether chemistry is well-known as well. Moreover, since the role of cyclic ethers in the broader chain-branching process is unknown, approximations used in chemical kinetics mechanisms lead to non-negligible uncertainty on predictions of global observables such as ignition delay times.

Typically, six-membered ROO ⟶ QOOH transition states have the lowest free energy among the ROO ⟶ QOOH H-transfer reactions.[1,12–14,22] The ensuing QOOH decomposition step yields a 4-membered cyclic ether, i.e. a substituted oxetane:

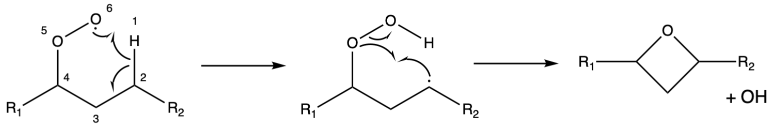

These substituted oxetanes are abundant in low-temperature combustion systems. For instance, Bugler et al.[15] conducted jet-stirred reactor experiments on *n*-pentane oxidation and detected six cyclic ether isomers, among which 2,4-dimethyloxetane (DMO) is the second most abundant. DMO has two diastereomers, *syn*-DMO and *anti*-DMO as shown here (note that the carbon atoms in the rest of the paper will be referred as they are labeled in this scheme):

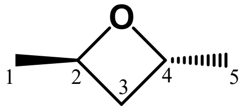

***anti*-DMO**

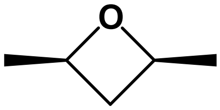

***syn*-DMO**

Current combustion mechanisms typically treat consumption reactions of oxetanes using a single step that is initiated by one of several radicals, e.g. OH, HO_2, or CH_3. For example, Table 1 lists the consumption reactions and rate coefficients for DMO prescribed in the *n*-pentane mechanism of Bugler et al.[15] Similar treatment is used in other combustion mechanisms, for instance for hydrocarbons[23–25] and for biofuels.[26,27] In Table 1, each reaction involves H-abstraction of one of the tertiary hydrogens in DMO and simultaneous scission of two bonds in the oxetane ring. The prescribed reactions assume two product channels with a branching ratio of 1:1, independently of the abstractor, OH or HO_2. However, these are not elementary reactions and neglect the formation of cyclic ether radical isomers and subsequent ring-opening or reaction with O_2. Moreover, stereochemistry is not taken into account, even though it directly influences the availability of certain reaction pathways and, as a result, branching fractions of products[18] and rates of chain-branching.[28]

Table 1 All reactions consuming 2,4-dimethyloxetane included in the latest *n*-pentane chemical kinetics model by Bugler et al.[15] are shown with their assigned rate coefficients. Both would involve simultaneous H-abstraction by some radical X and breaking two bonds in the oxetane ring.

Reaction	X	A (L mol^{-1} s^{-1})	n	E_a (cal/mol)
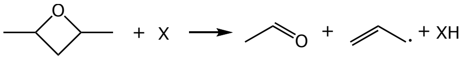	OH	2.26×10^3	2.73	-4688.6
	HO_2	1.72×10^1	3.46	$+9733.3$
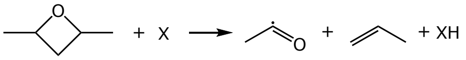	OH	2.26×10^3	2.73	-4688.6
	HO_2	1.72×10^1	3.46	$+9733.3$

Similarly to discrepancies with other chemical kinetics model predictions of cyclic ether concentrations,[16,29,30] Bugler et al.[15] show the largest discrepancy between modeled and experimental DMO mole fractions occurring at 10 atm and between 775 and 900 K, where its concentration is overpredicted by orders of magnitude. The disparity between the measurements and the model predictions is potentially due to incomplete cyclic ether sub-mechanisms. For example, H-abstraction followed by reaction with O_2 may account for a substantial portion of the DMO consumption reactions and may also contribute to the radical pools of OH and HO_2. Refined treatment of DMO chemistry may also resolve model discrepancies with other partially oxidized intermediates that are formed via reactions of DMO with O_2.

Because of the two diastereomers of DMO, stereochemical details may be crucial to consider,[18,31] and the size and structure of DMO offers perhaps just the right amount of complexity to understand the impact of stereochemical differences on reaction pathways. Studying this molecule can provide an outlook to the challenges that these yet unexplored chemistries offer, and perhaps motivate experimental techniques to try to capture ever so fine, yet important, details of chemical reactivity.

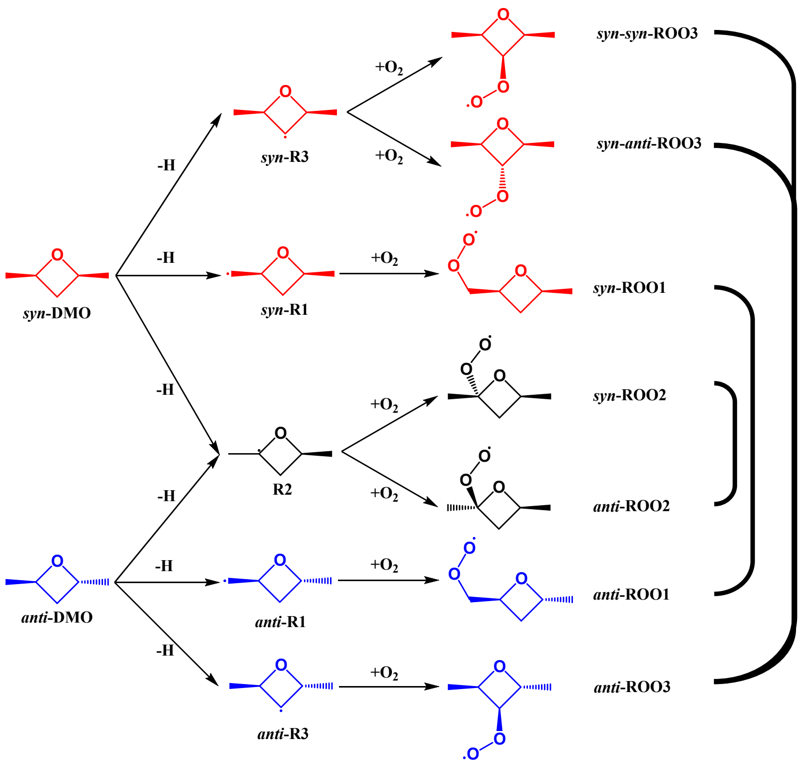

Fig. 1 H-abstraction of *syn*- and *anti*-DMO can yield five different R radicals. O_2-addition to those radicals can yield seven different peroxy radicals. H-abstraction from either of the tertiary carbons of *syn*- or *anti*-DMO produces a nearly planar radical, resulting in a loss of stereochemistry. The stereochemistry of the peroxy radical is dependent on the side to which O_2 adds for R2 and *syn*-R3. Peroxy radicals that are diastereomers are linked by black curves on the right.

The two diastereomers of DMO lead to five DMO radicals labeled *anti*-R1, *syn*-R1, R2 (tertiary radical that yields the same radical from both stereoisomers), *anti*-R3, and *syn*-R3 as shown in the center column of Figure 1, where the labeling refers to the carbon number from which the H atom was abstracted. Because O_2 can add to either side of the ring on *syn*-R3 and on R2, O_2-addition results in seven different 2,4-dimethyloxetanyl-peroxy radicals shown in the last column of Figure 1.

In this work, unimolecular reactions of all seven resultant cyclic ether peroxy radicals formed by O_2-addition to 2,4-dimethyloxetanyl isomers are characterized with KinBot,[32] an automated PES exploration and kinetics workflow software. In addition, temperature- and pressure-dependent rate coefficients are computed for the discovered reactions, which include QOOH ring-opening and rearrangement reactions beyond the typical ROO/QOOH chemistry. Particular attention is paid to the role of stereochemistry by accounting for *syn* and *anti* conformers to shed light on the importance of stereochemistry in these systems. Danilack et al.[28] have shown that accounting for diastereomers in the low-temperature oxidation of diethyl ether enhanced the reactivity of the original mechanism by 15%. Here, the impact of diastereomers is expected to be less subtle, due to the more sterically restrained ring structure, which can exclude entire pathways rather than simply elevating the barrier height.

There have been only a few direct theoretical studies of cyclic ether radical $+O_2$ reactions. These concerned tetrahydrofuran[33] and tetrahydropyran.[20,34,35] However, while these molecules are cyclic ethers, they are less likely to appear as a product in low-temperature autooxidation mechanisms. Moreover, tetrahydrofuranyl and tetrahydropyranyl radicals do not form stereoisomers when reacting with O_2.

Our paper is organized as follows. Section 2 provides details of the computational methods. Section 3.1 describes the reaction mechanisms of all seven ROO radicals grouped by reaction classes, followed by the results of the master equation calculations along with example yield determinations in section 3.2. Section 4 summarizes the results and gives an outlook for the implications of our results on combustion modeling and experiments.

2 Computational Methods

The reactive stationary points on the PESs of the seven cyclic ether peroxy radicals were explored and characterized automatically with our open-source kinetics workflow code, KinBot.[32,36] KinBot automatically explores reactive PESs using general templates, which were shown to be very effective for systems similar to the current one.[37–39] KinBot constructs good saddle point guesses in a series of constrained optimization steps at the L0 = AM1 level, which are then refined to a true first order saddle point (FOSP). The FOSPs are confirmed to be valid using intrinsic reaction coordinate (IRC) calculations. Previous versions of KinBot only tested the validity of a

FOSP based on the connectivity of the IRC endpoints. For the purposes of this work we implemented an additional test that assigns a stereochemical label to each atom in the reactant and compares them to the labels of the structure that arises from the IRC. This procedure only allows pathways where the stereochemistry is preserved.

KinBot calculations are initiated from a well. Wells discovered are followed further if the FOSP is lower than a user defined threshold. In this work we initiated seven KinBot calculations, one in each ROO well. We set the threshold for including a channel at the $R + O_2$ asymptote, as it is customary when $R + O_2$ systems are investigated. However, such a threshold was still too inclusive, because occasionally a very large number of chemical reactions were found. This happened typically when either a very exothermic reaction step was found, or in a ring-opening step, where the ring-opened product is an unsaturated acyclic product with three oxygen atoms. An unusually rich chemistry for similar reasons was also found with KinBot when the reaction of the triplet oxygen atom with cyclopenten was investigated.[40] To overcome the computational burden of the exploration of the likely unimportant chemistry and to aid the interpretation of the data, we, therefore, applied a second threshold criterion: we only followed a reaction pathway if it had >5% branching fraction in the high pressure limit at 400 or 1000 K at the L2 level. This eliminated a great deal of reactions channels. To show the extent of this issue, we placed some examples of potential energy search results in the ESI.

The reaction search, conformational analysis, and IRC calculations were performed at the L1 = B3LYP/6-31G level of theory. We did an exhaustive conformational search on a 60° grid (6 points). Ring conformers were generated by distorting the backbone of the ring systematically. When determining the number of ring conformers to generate, the following rules were used. For 3-member rings, no ring conformers were generated. For 4-, 5-, and 6-member rings we calculated the number of trial ring conformers as $3^{n_{\mathrm{ring}}-3}$, where n_{ring} is the size of the ring. For fused rings, the set of complete but smallest rings is taken. The conformers of each subring are sampled as usual. Finally, the conformers of the acyclic side chains of each ring conformer are then sampled on the 60° grid, yielding $n_{\mathrm{dih}}^3 \times \Pi_i^N 3^{n_{\mathrm{ring},i}-3}$ trial conformers overall, where N is the number of the subrings. However, if the predicted number of conformers were > 300, we randomly sampled 300 points on the grid. Moreover, if during the dihedral scans (see below) KinBot found a lower energy conformer, the new, lower energy structure replaced the old one. We allowed for at most three such substitutions, and in general, this happened rarely.

The lowest energy conformers were reoptimized at the L2 = ωB97X-D/6-311++G(d,p) level to obtain accurate geometries and harmonic frequencies. Internal rotors of the lowest energy conformers were scanned at the L2 level in 15° increments. Each point along the dihedral scan was submitted as an independent job, where all degrees of freedom except the scanned dihedral were relaxed. Failed points were approximated using interpolation based on a Fourier fit. In addition to overall translation and external rotation the motion along the rotors at the minimum was also projected out from the Hessian to arrive at the reduced set of harmonic frequencies. Final energies were obtained at the L3 = CCSD(T)-F12/cc-pVDZ-F12a//ωB97X-D/6-311++G(d,p) level of theory. Applying a larger, triple-ζ basis set for our system was not feasible. However, our own tests for slightly smaller, 7-heavy atom systems with similar chemistry show that the difference between CCSD(T)-F12/cc-pVDZ-F12a and CCSD(T)-F12/cc-pVTZ-F12a energies are well within 1 kcal/mol. We diagnosed large multireference characters via the T1 diagnostic.[41,42] The external and internal rotational symmetry numbers and the number of enantiomers for each stationary point are determined automatically by KinBot[32] as necessary for kinetics.[43,44]

Temperature- and pressure-dependent rate coefficients were calculated using a time-dependent chemical ME. To estimate the Lennard-Jones parameters, σ and ε (the equilibrium distance and the well depth, respectively) and the average downward energy transfer parameter $\alpha =< \Delta E_{\mathrm{down}} >$, we used the formulas of Jasper.[45] We evaluated σ and ε for Ar, which is likely a good estimate for N_2 as well,[45] using the formulas for hydroperoxides ($N = 8$), which are also a good substitute for more complex oxygenates,[45] like ours, and obtained $\sigma = 4.62$ Å and $\varepsilon = 248$ cm^{-1}. For the ROO1 and ROO2 species the effective atom number is $N_{\mathrm{eff}} = 4$, while for ROO3 $N_{\mathrm{eff}} = 2\frac{2}{3}$. We calculated α between 300 and 1000 K, and fitted it with a form $\alpha_0 \times (T/300\ \mathrm{K})^n\ \mathrm{cm}^{-1}$. We obtained $\alpha_0 = 269$ cm^{-1} and $n = 0.543$ for ROO1 and ROO2, and $\alpha_0 = 211$ cm^{-1} and $n = 0.659$ for ROO3, in both cases the RMS of the fit was ~ 6 cm^{-1}. We assumed the same energy transfer parameters for all wells on a PES. Significantly, for the QOOH species the estimates would be exactly the same, because the connectivity of the heavy atoms, which is used to evaluate N_{eff} is unchanged. Furthermore, since only N, the number of heavy atoms, enters the estimation of σ and ε, their estimates within this framework are also unchanged for ring-opened or otherwise rearranged structures. For Ar we used $\sigma = 3.462$ Å and $\varepsilon = 88.75$ cm^{-1}.[46]

The $R + O_2$ entrance channel on the PESs is barrierless. While in principle it is possible to calculate the microcanonical rate coefficients for this step in a variable-reaction-coordinate transition state theory (VRC-TST) framework, here we used a simpler approach and approximated the sum of states for the transition state using phase-space theory. The R...O_2 potential was modeled as ar^n, with $n = 6$. We adjusted the pre-exponential factor a to match the desired capture rate coefficient, which was $k_{300\ \mathrm{K}} = 7.5 \times 10^{-12}$ cm^{3}molecule^{-1}s^{-1} for both R1 species based on 1-butyl $+ O_2$,[47] $k_{298\ \mathrm{K}} = 1 \times 10^{-11}$ cm^{3}molecule^{-1}s^{-1} for both R2 species based on *tert*-butyl $+ O_2$ (we took half of the recommended value because of the two sides of possible attack are treated separately),[47] and $k_{298\ \mathrm{K}} = 1.5 \times 10^{-11}$ cm^{3}molecule^{-1}s^{-1} for *anti*-R3, and half of this value to each *syn*-R3 species $+ O_2$ reactions, based on cyclohexyl $+ O_2$ and cyclopentyl $+ O_2$.[48] Should direct determination for these barrierless processes arise, the ME given in the ESI can be easily adjusted.

The DFT calculations were done with the Gaussian 16,[49] while the coupled-cluster calculations with the Molpro 2020 program package.[50–52]. The input files for these programs were set up via ASE[53] as integrated into KinBot. The potential energy diagrams were made using the PESViewer code.[54] We solved the ME with the MESS code using the direct diagonalization method, which diagonalizes the global relaxation matrix.[55,56] The kinetic differential equations to calculate branching fractions was solved by the SciPy Python package's ODE integrator.

3 Results and Discussion

3.1 Potential energy surfaces and mechanism

The explored PESs – given the energy and branching fraction constraints – are provided in the ESI, where each PES is broken up into parts and color coded. A birds-eye view of the PESs already shows the striking differences in reactivity among these relatively similar ROO species. The *anti*-ROO3 species features just two wells and two bimolecular products, while the largest surface, the eventually combined ROO1 surface (see later) has 25 wells and 31 bimolecular product channels. In this section we summarize the mechanisms of the ROO radical decompositions and show summaries of the PESs. In general, the T1 diagnostic was below the thresholds. Important exceptions are mentioned in the following subsections and are listed as past of the ESI.

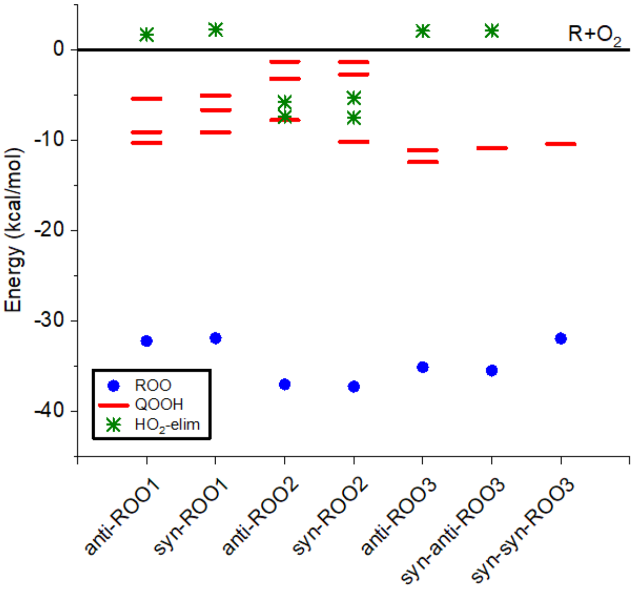

Fig. 2 ROO well depths and reaction barrier heights stemming from each initial ROO well. Energies are calculated at the L3 = CCSD(T)-F12/cc-pVDZ-F12a//ωB97X-D/6-311++G(d,p) level and include ZPE. The zero of energy is that of the respective $R+O_2$ asymptotes. Note that the HO_2-elimination channel for *syn*-*syn*-ROO3 is absent because of steric constraints.

3.1.1 Reactions of the ROO radicals

The seven ROO radicals can undergo the typical pathways: unimolecular dissociation to the $R+O_2$ reactants, direct HO_2-elimination, and isomerization to QOOH species.[1] These pathways are shown in the first, blue boxes in the ESI for each PES. A summary of our calculations for these initial steps are shown in Figure 2, displaying the well depth of the ROO radicals and the barrier heights grouped by reaction types leading out of these wells.

The deepest ROO wells are the ROO2 ones. Previous theoretical studies of alkyl-substituted oxirane peroxy radicals revealed similarly deep wells when the peroxy group is positioned on the same carbon as the ether group: 2,3-dimethyloxirane[18] and 2-ethyloxirane[57] had well depths ranging 39.3 – 40.8 kcal/mol. ROO radicals with peroxy groups positioned on the alkyl substituents had well depths ranging 29.2 – 32.9 kcal/mol, at the ccCA-PS3 level of theory.[58] In the present work, peroxy radicals with the peroxy group positioned on the alkyl substituents, *anti*- and *syn*-ROO1, had well depths of $\sim$ 32 kcal/mol. The peroxy group in the ROO3 radicals are positioned on the ring, but not directly adjacent to the ether group. While *syn*-*anti*-ROO3 and *anti*-ROO3 had similar well depths to the open chain well depth of $\sim$ 35 kcal/mol, *syn*-*syn*-ROO3 has a well depth of only 31.9 kcal/mol, likely due to steric hindrance of the two methyl groups and peroxy group.

All direct HO_2-elimination pathways have barriers higher than one or all QOOH isomerization pathways. Note that the HO_2-elimination channel for *syn*-*syn*-ROO3 is absent because the H atom is too far for the –OO moiety to reach. Furthermore, some of the HO_2 elimination channels, which were kept according to our rules at the L2 level, are above the $R+O_2$ asymptote when evaluated at the L3 level.

The isomerization pathways leading to QOOHs for the seven peroxy radicals are restricted by the stereochemistry of the peroxy radicals. For H-abstraction from a tertiary carbon to occur, the methyl group on that carbon must be on the opposite side of the ring to the peroxy group. For H-abstraction from a (primary) methyl group to occur, the methyl group must be on the same side of the ring as the peroxy group, unless the methyl group and the peroxy radical are on the same carbon. However, H-abstraction from the methyl group on the same carbon as the peroxy group usually have the highest accessible QOOH barriers. While H-abstraction from the secondary carbon is not restricted by stereochemistry in these radicals and the barriers are usually low, the QOOH wells are shallow and favor the reverse reaction to the initial peroxy radical (this can be seen in Figure 3).

Because of the steric constraints that the backbone's cyclic structure represent, the ring-size of the energetically lowest QOOH isomerization pathways vary a lot. The most favored ring size for for *syn*-ROO1 is 8, for *anti*-ROO2 and *anti*-ROO1 it is 7, for *syn*-ROO2, *anti*-ROO3, and *syn-syn*-ROO3 it is 6, and for *syn-anti*-ROO3 it is 5. The ROO/QOOH isomerization also leads to an interesting stereochemical outcome in the case of *anti*- and *syn*-ROO1 radicals, which are diastereomers, but their isomerization produces a chemically identical QOOH with one stereocenter only:

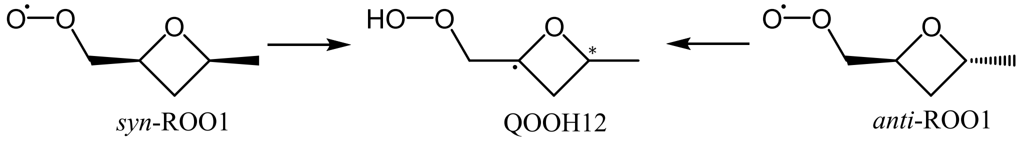

3.1.2 Reactions of the QOOH radicals

Conventional QOOH decomposition reactions play a significant role in the low-temperature chemistry of these cyclic ether peroxy radicals, as can be seen in the second, red boxes in the PESs presented in the ESI. The barrier heights stemming from the QOOH radicals are summarized in Figure 3. The naming convention of QOOH radicals is that the first number denotes the carbon to which the –OOH group is attached, while the second number denotes the location of the radical center. All expected HO_2-elimination pathways were found and had submerged barriers relative to the corresponding $R + O_2$. (Interestingly, the reverse barriers from $HO_2 +$ alkenes are very small, especially when the double bond formed was in the oxetane ring.) In all cases, however, there were other, energetically more favorable channels, as seen in Figure 3.

When cyclic ether loses an OH radical via cyclization, bicyclic ethers are formed. Pathways to bicyclic ethers + OH for our QOOH radicals have much lower barriers than in the previously studied 2,3-dimethyloxiranyl + O_2 and 2-ethyloxiranyl + O_2 systems,[18,57] and are frequently the lowest energy pathway or competitive with ring opening reactions. All expected bicyclic ether pathways were found by KinBot for all QOOHs except for *syn*-QOOH24 and *anti*-QOOH25; these pathways were excluded during the initial reaction search due to their barrier height ($\sim$ 32 kcal/mol). Bicyclic ether formation from QOOH is the lowest energy pathway for both the *syn-anti*-ROO3 and *anti*-ROO1 surfaces. Additionally, bicyclic ether formation was the lowest energy pathway for all three QOOH wells on the *anti*-ROO1 surface, two out of three QOOH wells on the *anti*-ROO2 and *syn*-ROO2 surfaces, and one of two QOOH wells on the *anti*-ROO3 surface. Several bicyclic ether formation TSs had high T1 diagnostics, ranging 0.055 to 0.061.

Each DMO QOOH radical has two potential ring opening pathways. Tertiary QOOH radicals can ring open to produce either a KHP radical by breaking the C-O bond or an unsaturated ether hydroperoxyalkyl radical by breaking the C-C bond. When the QOOH produced is alpha, OH is lost from the hydroperoxy group in the same step. Barriers to ring opening by C-O bond scission are usually lower in energy than for C-C bond scission. Primary QOOH radicals can ring open to produce either an unsaturated hydroperoxyalkoxy radical by breaking the C-O bond or an unsaturated ether hydroperoxyalkyl radical by breaking the C-C bond. Secondary QOOH radicals can ring open to produce two different unsaturated hydroperoxyalkoxy radicals, depending on which C-O bond is broken. However, the secondary QOOH radicals have shallow wells, so the reverse reaction to the initial cyclic peroxy radicals and bicyclic ether formation out-compete ring opening. Decomposition products for analogous radical species in oxidation of 2,3-dimethyloxirane and 2-ethyloxirane have been detected in previous studies.[18,57] However, the KHP-type radicals in the previous studies were resonance-stabilized vinoxy radicals,[18,57] while the KHP-type radicals herein have two carbons between the radical and the carbonyl, and are, therefore, not resonance stabilized. Note that several ring opening TSs had high (> 0.03) T1 diagnostics ranging 0.03 to 0.049 as listed in the ESI.

In total, twelve ring-opening pathways were kept after the 5% well branching fraction cutoff, three of which involved simultaneous OH loss. The lowest energy pathway for *anti*-ROO2 is ring-opening to a hydroperoxyalkoxy radical, 2-hydroperoxy-2-alkoxy-4-pentene, for *syn*-ROO2 it is simultaneous ring-opening and OH loss from *syn*-QOOH24, yielding acetylacetone. Finally, for *syn-syn*-ROO3 and *anti*-ROO3 the lowest energy pathway is simultaneous ring-opening via C-C bond scission and OH loss, yielding 2-(vinyloxy)propanal as shown in Figure 4.

As will be seen later, stereochemistry has a fundamental impact on the outcomes on these reactions: diastereomers produce very different products. Is this behavior predictable based on the barrier heights shown in Figure 3? There are several QOOH radicals, where the stereochemistry of the carbon sidechains, *syn* or *anti*, makes almost no difference for the barrier heights. These are QOOH12, QOOH13, QOOH21, QOOH32, and to some extent, QOOH23. These are radicals where the formation of the QOOH radicals and

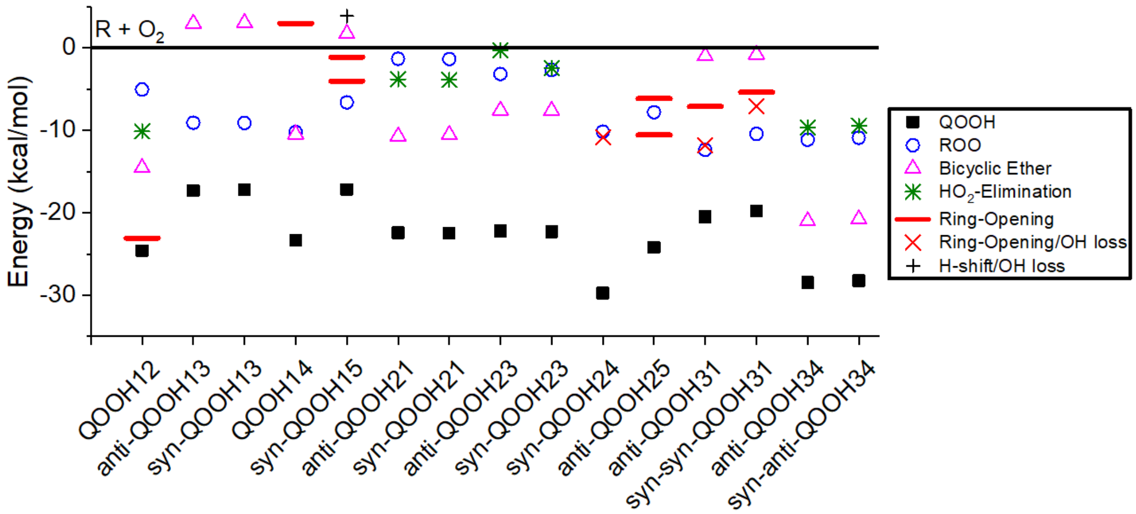

Fig. 3 QOOH well depths and reaction barrier heights stemming from each QOOH well. Energies are calculated at the L3 = CCSD(T)-F12/cc-pVDZ-F12a//ωB97X-D/6-311++G(d,p) level and include ZPE. The first digit after "QOOH" is the denotes the carbon (numbered from left to right) which is bonded to the peroxy group, and the second digit denotes the the carbon-centered radical site. The zero of energy is that of the respective R + O$_2$ asymptotes. QOOH12 is on both the *syn-* and *anti*-ROO1 surfaces, and is shown relative to *syn*-R1 + O$_2$ here

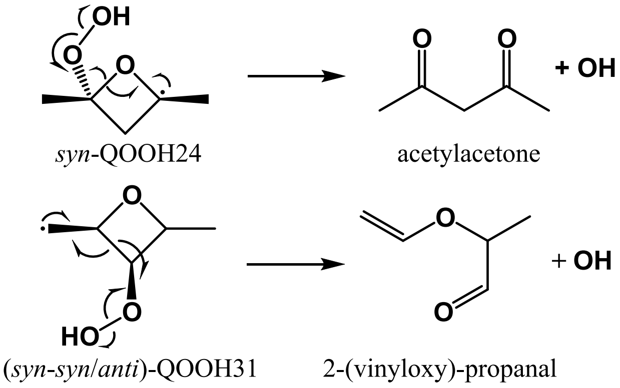

Fig. 4 Three ring opening reactions involves simultaneous loss of OH, yielding acetylacetone from *syn*-QOOH24 and 2-(vinyloxy)propanal from *syn-syn-* and *anti*-QOOH31.

their further reactions do not involve *both* stereocenters or ligands or where the pathways collapse onto each other from the starting diastereomers. However, QOOH14, QOOH15, QOOH24 and QOOH25 are radicals that only appear in one or the other diastereomer, and differences for QOOH31 are more significant, allowing the chemical reactivity to diverge significantly.

3.1.3 Reactions of ring-opened species

As stated above, the ring-opening reactions of QOOH radicals lead to hydroperoxyalkoxy radicals and unsaturated ether hydroperoxyalkyl radicals. These ring opened species often favor β-scission reactions producing small organic acids and radicals as shown in green boxes in the ESI. (Three of the transition states for β-scission of ring-opened QOOH radicals had high T1 diagnostics, ranging from 0.030 to 0.036.) An important detail is that the reverse of the ring-opening reactions leads to the scrambling of stereoisomers. However, we found that the forward reactions from these ring-opened species are order of magnitude more facile than ring closing, therefore, we have excluded the exploration of scrambling processes.

In addition to β-scission reactions, hydroperoxyalkoxy radicals can transfer the hydroperoxy group H to the alkoxyradical, producing a new peroxy radical, causing the surface to grow dramatically in complexity. The primary reactions for these new peroxy radicals are shown in magenta boxes in the ESI. Five such new peroxy radicals were discovered that account for more than 5% of the branching fraction from ring-opened QOOH wells. They were 1-peroxy-2-methyl-3-butanone on the *anti*-ROO1 surface, 2-(vinyloxy)-1-peroxypropane and 1-peroxy-2-hydroxy-4-pentene on the *syn*-ROO1 surface, 2-peroxy-2-hydroxy-4-pentene on the *anti*-ROO2 surface, and the resonantly stabilized 3-peroxy-4-hydroxypentene on the *syn-syn*-ROO3 surface. Most of these species that were followed further by KinBot were produced via a 6-membered transition state. Two of the H-transfer transition states had large T1 diagnostics, the ones leading to the resonantly stabilized 3-peroxy-4-hydroxypentene on the *syn-syn*-ROO3 surface (τ_1 = 0.104) and 2-peroxy-2-hydroxy-4-pentene on the *anti*-ROO2 surface (τ_1 = 0.059). The transition state forming 1-peroxy-2-hydroxy-4-pentene on the *syn*-ROO1 surface encountered convergence issues at L3, possibly due to similarly high multireference character. The chemistry of these new ROO radicals which are unsaturated and the R is also oxygenated can get very complex. For instance, on the *anti*-ROO2 and *syn*-ROO1 surfaces, ring-opened peroxy radicals have low barriers to form cyclic peroxy alkyl radicals by adding the terminal O in the peroxy group to the double bond. The corresponding parts of the PESs are shown in purple boxes in the ESI. Several of the transition states for cyclic peroxy radical decomposition had large T1 diagnostics, ranging 0.03 to 0.105.

KHP-type radical 1-hydroperoxypentane-4-one-2-yl from the *anti*-ROO1 surface can decompose via cyclic ether formation of 1,2-epoxypentane-4-one (16.4 kcal/mol barrier) or HO_2 elimination (15.2 kcal/mol barrier), leaving pent-4-en-2-one. Alternatively, 1-hydroperoxypentane-4-one-2-yl can undergo a rearrangement through a three-membered ring transition state (Figure 5) studied by Scheer et al. in a series of four-carbon ketones.[59] In experiments, the detection of the decomposition products of 1-hydroperoxypentane-4-one-2-yl may mistakenly suggest the presence of *iso*-pentane, as it could also be produced via H-abstraction of a KHP in the *iso*-pentane mechanism from Bugler et al.[60]

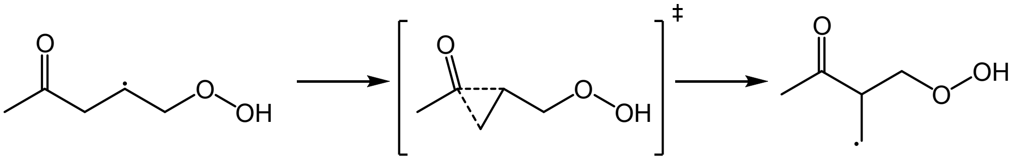

Fig. 5 The shown KHP-type radical from the *anti*-ROO1 surface can undergo rearrangement as described by Scheer et al.[59] The barrier height is 16.4 kcal/mol. This reaction competes with a bicyclic ether formation of 1,2-epoxypentane-4-one with a barrier height of 15.2 kcal/mol barrier and HO_2 elimination, leaving pent-4-en-2-one. This radical could also be produced by H-abstraction from a KHP in the mechanism for low-temperature oxidation of *iso*-pentane.[60]

3.1.4 Stereochemistry-dependent mechanisms

We presented a large number of potentially important pathways in the previous sections. Here we focus on the overall lowest energy pathways starting from each ROO radical, and show how they differ for the different diastereomers using the grouping shown in Figure 1. The pathways shown herein start from the $R + O_2$ entrance, follow the lowest exit channel from the available forward reaction pathways until a bimolecular exit is reached.

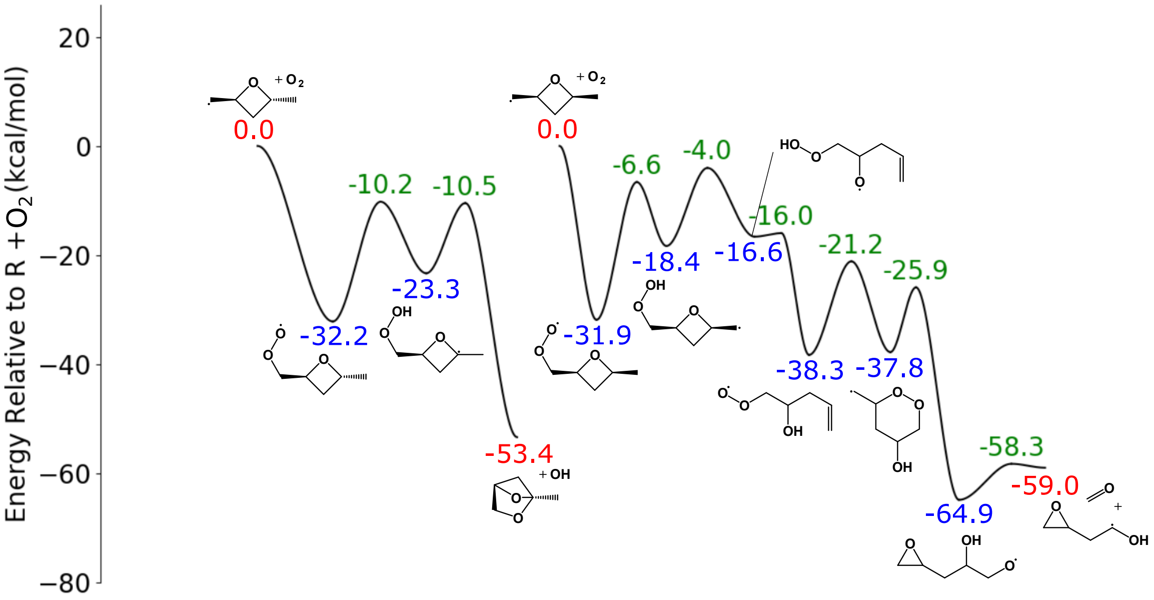

Fig. 6 Lowest energy pathways for the two ROO1 radicals at the L3 level, including ZPE. The pathway shown for *anti*-ROO1 (left) is the lowest energy pathway on the surface, which produces a bicyclic ether.The pathway shown for *syn*-ROO1 (right) yields formaldehyde and an epoxide radical. The barrier height of -16.0 kcal/mol is at the ωB97X-D/6-311++G(d,p) level of theory due to convergence issues with CCSD(T)-F12/cc-pVDZ-F12.

R1 has two diastereomers, *syn*-R1 and *anti*-R1 which produce two diastereomers of the peroxy radical ROO1, *syn*-ROO1 and *anti*-ROO1. The lowest energy pathway for *anti*-ROO1 (Figure 6) is internal H-abstraction from the distal tertiary carbon, forming QOOH14, which has a low energy barrier (12.8 kcal/mol) to bicyclic ether formation. The lowest energy pathway that leads to bimolecular products for *syn*-ROO1 is internal H-abstraction from the distal methyl group, forming *syn*-QOOH15. *syn*-QOOH15 ring-opens via C-O bond scission, forming an unsaturated hydroperoxyalkoxy radical. The energy barrier to transfer H from the hydroperoxy group to the alkoxy group is less than 1 kcal/mol, forming a new peroxy radical. Note that despite various trial guess HF wavefunctions the L3 energy computations of this transition state did not converge, therefore, we used the L2 barrier height here and in the ME. The new peroxy radical has a low barrier to form a cyclic peroxy radical, which decomposes to an epoxide radical and formaldehyde in two steps. Overall, the two stereoisomers behave in distinctly different ways, *anti*-ROO1 follows more of an expected ROO/QOOH chemistry, while *syn*-ROO1 has a more unusual chemistry dominated by ring-opening. It should also be noted that for the two ROO1 species the explored pathways had shared species (see the end of section 3.1.1, therefore, in the ME treatment (see section 3.2) the two surfaces had to be merged.

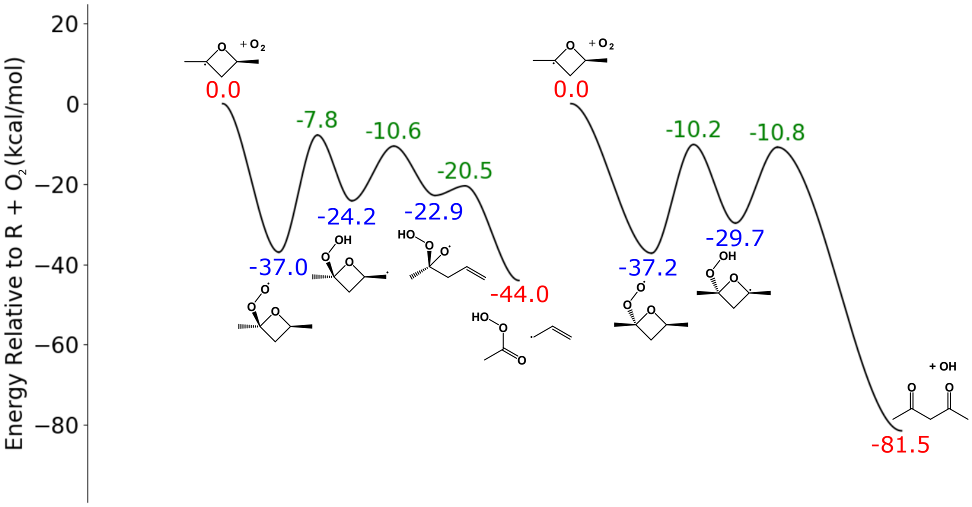

Fig. 7 Lowest energy pathways for the two ROO2 radicals at the L3 level, including ZPE. The lowest energy path for *syn*-ROO2 (left) is internal H-abstraction from the distal tertiary carbon, followed by simultaneous ring-opening and OH loss, giving acetylacetone. The lowest energy path for *anti*-ROO2 (right) is internal H-abstraction from the distal methyl group, followed by ring opening by C-O bond scission to produce a hydroperoxyalkoxy radical, which decomposes to peracetic acid and allyl radical.

O_2-addition to R2 can lead to two different cyclic ether peroxy radicals, *syn*-ROO$_2$ and *anti*-ROO$_2$ (Figure 7). The lowest energy pathway for peroxy radical *anti*-ROO2 is internal H-abstraction, giving a primary QOOH radical, with the radical center on the distal methyl group. H-abstraction from the distal tertiary carbon is restricted by stereochemistry. This QOOH ring opens to form a hydroperoxyalkoxy radical, which has a low barrier to β-scission. The products are allyl radical and peracetic acid, a small, closed-shell KHP molecule. Peracetic acid is the second-most abundant organic peroxide in the troposphere, where it contributes to organic aerosol formation and aging.[61–65] The lowest energy pathway for peroxy radical *syn*-ROO2 is internal H-abstraction from the distal tertiary carbon (H-abstraction from the distal methyl group is restricted by stereochemistry). The formed QOOH radical ring opens along the C-O bond and forms acetylacetone (see also Figure 4). Overall, while both ROO2 radicals seem to favor ring-opening pathways, *anti*-ROO2 has a more direct route towards OH production. The small KHP formed in the case of *syn*-ROO2 is relatively stable, the O–O bond is about 40 kcal/mol.[66]

Finally, The pathways starting in R3 are compared in Figure 8. O_2-addition to the *syn*-R3 leads to two different cyclic ether peroxy radical wells, *syn*-*syn*-ROO3 and *syn*-*anti*-ROO$_3$. Peroxy radical *syn*-*syn*-ROO3 undergoes internal H-abstraction from one of the methyl groups, giving a primary cyclic ether QOOH radical. H-abstraction from the tertiary carbon is restricted by the stereochemistry. The lowest energy pathway from this QOOH other than isomerization to the initial peroxy radical is simultaneous ring opening and OH loss, forming 2-(vinyloxy)propanal. Peroxy radical *syn*-*anti*-ROO3 undergoes internal H-abstraction from one of the tertiary carbons, giving a tertiary cyclic ether QOOH radical. H-abstraction from the methyl groups is restricted by stereochemistry. The lowest energy pathway from this QOOH is OH loss forming the bicyclic ether, 1,3-dimethyl-2,5-dioxabicyclo[2.1.0]pentane. Finally, the peroxy group in *anti*-ROO3 can abstract from the methyl group or the tertiary carbon; however abstraction from the methyl group is the lowest energy path, resulting in the same product as *syn*-*syn*-ROO3, 2-(vinyloxy)-propanal. Overall, either via bicyclic ether formation or ring opening, ROO3 radicals tend to produce OH.

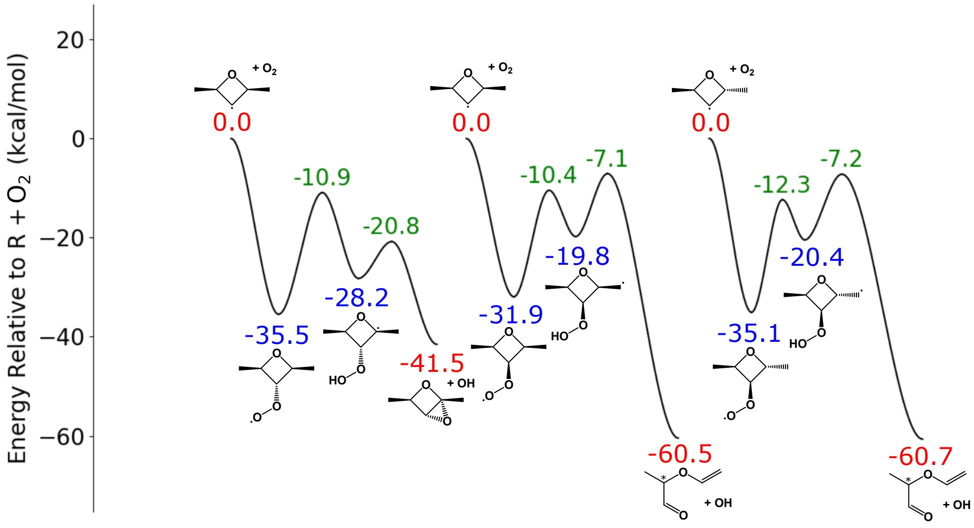

Fig. 8 Lowest energy pathways for the three ROO3 radicals at the L3 level, including ZPE. The lowest energy path for *syn*-*anti*-ROO3 (left) is internal H-abstraction from one of the tertiary carbons followed by bicyclic ether formation. The lowest energy path for *syn*-*syn*-ROO3 (center) and *anti*-ROO3 (right) is internal H-abstraction from one of the methyl groups followed by simultaneous ring-opening by C-C bond scission and OH loss.

3.2 Kinetics and product yields

We calculated rate coefficients for more than 4,000 reactions, from which about 3,000 originate from the large combined ROO1 PES. The reason for the large number is because the ME provides results for both direct and well-skipping reactions, and that way it connects all species with each other. While the largest computational cost is the exploration and characterization of the PES, solving the ME for the 25-well and 31-bimolecular product ROO1 system is not fast: it takes 1–3 hours on a 48-core computing node for one pressure-temperature condition. The time-consuming step is the diagonalization of the transition matrix, and the run times are longer for low temperatures and high pressures, where the elements of the transition matrix span a larger range (chemistry is slow, while collisional energy transfer is fast). Each of the ∼4,000 rate coefficients were evaluated for eight temperatures (300–1000 K) and five (7.6–76000 Torr) pressures, totaling in about 160,000 rate coefficient values. These can be found in the ESI. In the following we show some select results to shed light on the expected behaviour of our cyclic ether systems.

As mentioned in section 3.1.3, there are several new acyclic ROO radicals that appeared during the search. We used the same phase-space-theory-based approach as described in section 2 for the entrance channels. To approximate the 300 K capture rate coefficient for the new ROO radicals on the ROO1 PES we used 7.5×10^{-12} cm^3 molecule^{-1} s^{-1},[47] on the *anti*-ROO2 PES we used 3×10^{-11} cm^3 molecule^{-1} s^{-1},[67] and on the *syn*-*syn*-ROO3 PES, where the new ROO radical is resonance stabilized, we used 7.5×10^{-13} cm^3 molecule^{-1} s^{-1}.[68]

3.2.1 Unimolecular rate coefficients starting in the ROO wells

Figure 9 shows the most important unimolecular rate coefficients starting in the ROO well as a function of temperature at 760 Torr, for each of the seven cyclic ether peroxy radicals studied in the present work. The reactions are color-coded based on the products or intermediates to which they correspond. Well skipping reactions, i.e., reactions connecting non-neighboring species,[69,70] were found to be fast enough to be important for all systems even at 760 Torr, especially at higher temperatures. These reactions are marked with a dashed line in Figure 9. The line color of a well-skipping pathway is the same as the color of the sequential reaction corresponding to the skipped well to easily visualize the competition between collisional stabilization and chemical reactions. The temperature at which the well skipping reactions overtake the reactions to their respective wells are marked in Figure 9 for *anti*-ROO2 and *syn*-ROO2. Note also that some of the rate coefficients vanish above certain temperatures. This is due to fast equilibration between pairs of species (wells and/or bimolecular products) that happens on timescales faster than collisional relaxation. It leads to merging, where the merged species cannot anymore be considered as separate in a kinetic sense.[69]

As expected, dissociation rate coefficients back to $R + O_2$ are very similar for diastereomeric species. However, the competition with the rest of the channels is very different for diastereomers. For instance, *anti*-ROO1 is governed by a mix of ring-opening and QOOH isomerization reactions, while *syn*-ROO1 is dominated by ring-opening reactions only. HO_2-elimination rate coefficients were approximately two orders of magnitude larger for *syn*- and *anti*-ROO2 than for the remaining cyclic ether peroxy radicals. Yet, there is a strong contribution from QOOH isomerization channels for *syn*-ROO2 that is largely absent for *anti*-ROO2. Considering the similarities in barrier heights for the *syn* and *anti* versions of QOOH21 and QOOH23 (see Figures 2 and 3) it is not surprising that their kinetics are also very similar. The difference between the two diastereomers stem from the presence and absence of the the QOOH25 and QOOH24 routes, the latter strongly competing with the HO_2-elimination pathways.

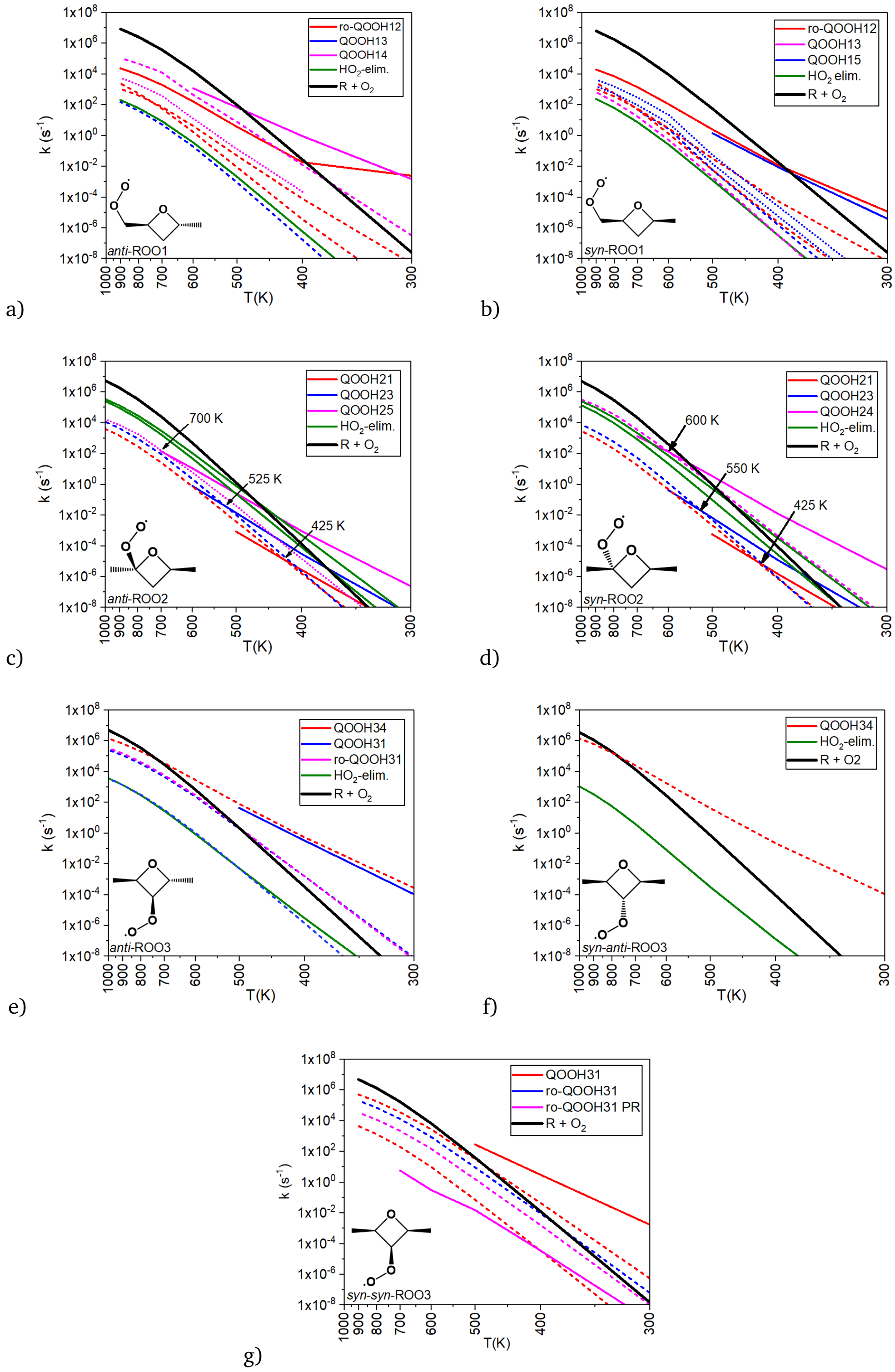

Fig. 9 The highest several rate coefficients for each of the seven 2,4-dimethyloxetane (DMO) peroxy radicals are given as a function of temperature. Well-skipping rate coefficients are denoted by dashed lines in the same color as the well skipped. For *anti*-ROO1 and *syn*-ROO1, ro-QOOH12 denotes the ring-opened QOOH12 KHP-type radical, 1-hydroxypentan-2-one-4-yl. For *syn*-ROO1, there are dotted and dashed blue lines denoting two different ring opening products of *syn*-QOOH15. For *anti*-ROO2 (c) and *syn*-ROO2 (d), the temperatures at which the well-skipping rate coefficients overtake the rate coefficients for its well are pointed out by arrows. For *anti*-ROO3 (e) and *syn-syn*-ROO3 (g), ro-QOOH31 denotes the ring opened *anti*-QOOH31 species, 3-hydroperoxy-2-alkoxypentane-1-yl. For *syn-syn*-QOOH31 (g), ro-QOOH31 PR denotes the peroxy radical, 3-peroxy-2-hydroxypentane, which is formed via internal H-transfer of ro-QOOH31.

The three ROO3 diastereomers have two QOOH wells, QOOH31 and QOOH34. While *syn-anti*-ROO3 only has QOOH34 and *syn-syn*-ROO3 only has QOOH31, *anti*-ROO3 has both. Furthermore, the rate coefficients for the pathways through QOOH34 or QOOH31 are nearly identical for these diastereomer pairs. This is because these particular transition states involve only one side of the molecule, making the position of the opposite methyl group relatively inconsequential. For *anti*-ROO3, which can form both QOOH31 and QOOH34, the QOOH34 pathway forming a bicyclic ether + OH wins. The steric hinderance in *syn-syn*-ROO3 is stronger than in any of the other two, yielding a shallower well (see Figure 2) and consequently a faster ROO $\longrightarrow$ $R + O_2$ dissociation rate coefficient. In fact, the dissociation of *syn-syn*-ROO3 to R + O_2 has the largest rate coefficient for all temperatures higher than ∼500 K at 760 Torr. As mentioned earlier, the other consequence of the steric hinderance is the absence of the HO_2-elimination channels.

It is also interesting to see that the QOOH radicals cease to exist in a kinetic sense just slightly above the temperatures where well-skipping ROO $\longrightarrow$ products reactions become faster than the sequential ROO $\longrightarrow$ QOOH ones in the ROO2 case. What is remarkable about the ROO3 and ROO1 systems is the dominance of the well-skipping pathways. It is not caused by a single low barrier in these systems, rather a combination of a series of low barriers and shallow wells relative to the other four peroxy radicals. Such kinetic behavior means that at 760 Torr the lifetime of the population in the QOOH wells is very short, but also means that most of this ephemeral population exists in a rotationally and vibrationally highly excited state. Whether the fleeting QOOH population can participate in so-called second-O_2-addition processes to a significant extent is unknown at this point and warrants further detailed studies.

3.2.2 Product yields starting from the $R+O_2$ reactants

Here we present the product yields for two typical experimental conditions that could guide experimentally investigations of these systems, for instance, in a Cl-atom initiated oxidation experiment of DMO. Figure 10 shows the $R+O_2 \longrightarrow$ product yields at 760 Torr and at 650 K and 825 K under pseudo-first-order conditions, $[O_2] = 10^{18}$ molecule cm^{-3}, at $t = 20$ ms reaction time. Integrating the kinetic differential equations take into account all reactions pathways, both direct and well-skipping ones. Because of the wide variety of the products, here we focus on two important questions only. First, we are interested in the ring-opening propensity of the various $R+O_2$ systems; this is shown by the balance of the black (HO_2 elimination) + red (bicyclic ether) to the blue (ring opening) bars. Second, we are also interested in the propensity of these systems to promote autoignition or delay it. Therefore, we marked the ring-opening channels with shades of blue to indicate whether they form OH, HO_2, or neither.

HO_2 elimination is important for the ROO2 peroxy radicals only. As seen in Figure 2, the direct HO_2 elimination barriers for these two species are lower than that for the ROO1 or ROO3 radicals, and indeed, this is the main reason why these reactions yield a lot of HO_2. Nevertheless, the difference between *syn*- and *anti*-ROO2 is large. The reasons for this is the lower barrier to isomerization in *syn*-ROO2 (Figure 2). For this species the remainder of the flux goes to ring-opening products, which end up making acetylacetone as was shown in Figure 4. The branching fraction for acetylacetone decreases from 64% at 650 K to 42% at 825 K, and can be explained by the combination of entropic and enthalpic contributions to the barrier heights. It is notable that the most abundant product on the *syn*-ROO2 surface is acetylacetone, which is under-predicted by the model built by Bugler et al.[15] by over a factor of two for equivalence ratios greater than 1.0.

The ROO3 species show an array of behavior: *syn-syn*-ROO3 mostly produces OH radicals via ring-opening reactions, while *syn-anti*-ROO3 produces OH radicals in bicyclic ether reactions. While in terms of the OH-balance, *anti*-ROO3 also produces exclusively OH radicals, it is an intermediate case, where we see both cyclic ether and ring opening pathways. Again, this is in accordance with the lowest energy pathway diagrams in Figure 8. The branching fractions in this case change only marginally with temperature. The major products for *anti*-ROO3 and *syn-anti*-ROO3 are a bicyclic ether, 1,3-dimethyl-2,5-dioxabicyclo[2.1.0]pentane, and OH, which were the bimolecular products of the lowest energy pathway for *syn-anti*-ROO3. The major products for *syn-syn*-ROO3 are 2-(vinyloxy)propanal and OH, which are the bimolecular products of the lowest energy path.

Finally, the ROO1 system shows yet a different behaviour. First, in contrast to the other two groups (ROO2 and ROO3), the branching fractions have a stronger temperature dependence. The *syn*-ROO1 case exclusively ring opens at 625 K, while there is about 10% byciclic ether formation at 825 K. Moreover, the ring opening pathways produce non-OH and non-HO_2 radicals to a larger extent, about 40%, at the higher temperature. The dominance of ring opening is in accordance with Figure 6. The major ring-opened products for *syn*-ROO1 are 5-methyldihydrofuran-3(2H)-one, which is formed from the ring-opened QOOH12 KHP-type radical, 1-hydroperoxypentan-2-one-4-yl. This species is not the same as the one shown in Figure 6 at the end of the ring opening channels, because the closeness of the barrier heights on this PES to the various QOOH radicals results in competition that is ultimately decided by free energy differences, rather than purely enthalpic ones. *anti*-ROO1, as illustrated in Figure 6, is much less likely to ring open, and forms a lot of bicyclic ethers, mostly 1-methyl-2,5-dioxabicyclo[2.1.1]hexane from *anti*-QOOH14.

4 Conclusions

In this work we have, for the first time, established the mechanism and kinetics for the low-temperature autooxidation chemistry of an important cyclic ether species, 2,4-dimethyloxetane (DMO). DMO exists in *syn* and *anti* forms, and the H-abstraction and O_2-addition channels lead to three groups of diastereomers, a total of seven organic ether peroxy radicals. We tackled the problem's complexity with our automated kinetics workflow code, KinBot that allowed the exploration and characterization of the reactive PESs.

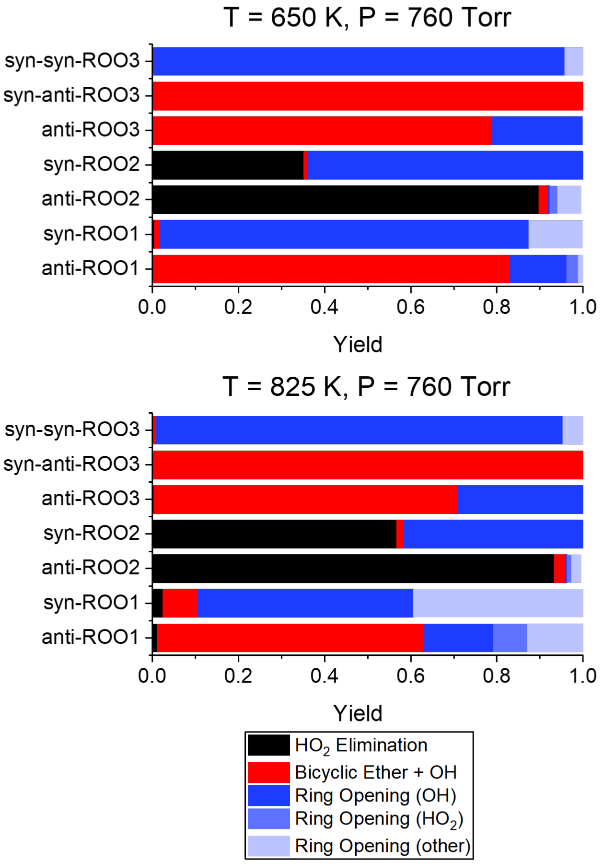

Fig. 10 $R + O_2 \longrightarrow$ products yields at 760 Torr and at 650 K (top) and 825 K (bottom) under pseudo-first-order conditions, $[O_2] = 10^{18}$ molecule cm^{-3}, and $t = 20$ ms.

We found a plethora of possible pathways beyond the usual ROO/QOOH chemistry due to ring-opening steps. Four out of the seven cyclic ethers produce largely OH radicals, contributing to chain propagation, while one of them mostly just forms HO_2 radicals, slowing down the ignition process. The remaining two produce both OH and HO_2 radicals. While HO_2 formation is linked to the direct HO_2 elimination pathway generally characteristic of hydrocarbon oxidation at low temperatures, OH in these systems is linked both to bicyclic ether formation and ring opening.

Stereochemistry has dramatic impact on the product yields due to steric hinderances. Diastereomeric radical pairs in our investaigate set behave differently, switching entirely between ring opening or bicyclic ether formation, or forming radically different fractions of OH vs. HO_2 radicals. Because stereochemistry so strongly influences the product yields, it remains extremely difficult to assess the importance and role of cyclic ethers in low-temperature combustion systems in general. Nevertheless, simplified treatments of cyclic ethers in combustion mechanisms can clearly lead to errors in ignition delay predictions and can mislead experiments that try to trace KHP formation back to the presence of dicarbonyls.

We calculated pressure- and temperature-dependent rate coefficients for the important parts of the PESs stemming from the seven initial ROO radicals using a multiwell master equation model in Ar bath gas between 300 and 1000 K temperatures and 7.6 and 76,000 Torr pressures. The rate coefficients can be used in combustion models to reduce uncertainties due to the secondary chemistry of cyclic ether. Besides being able to better predict OH and HO_2 yields, our rate coefficients can also help better quantify QOOH radicals, the parents of cyclic ethers, and KHPs, which may have overlapping chemistry with cyclic ethers. O_2-addition to alkyl-substituted oxirane radicals can similarly lead to KHP-type radicals or dicarbonyls, through ring-opening of cyclic ether QOOH radicals.[18,57] We have for instance shown that the the detection of the decomposition products of 1-hydroperoxypentane-4-one-2-yl may mistakenly suggest the presence of *iso*-pentane, as it could also be produced via H-abstraction of a KHP in the *iso*-pentane mechanism from Bugler et al.[60]

Together with previous work on the mechanisms of similar systems[18,20,33,57] it is clear that qualitative understanding of cyclic ether autooxidation remains a complicated task. Automated tools, such as KinBot, are expected to play a pivotal role in exploring these yet unknown chemical reactions. The greatest challenge we found when exploring our system is the plethora of pathways. While automated tools help reveal them, it is difficult to keep the search both unbiased yet focused on the chemical questions at hand. We generated rate coefficients for about 4,000 reactions, but a thorough analysis and meaningful use of the data might require the development of further computational tools.

Conflicts of interest

There are no conflicts to declare.

Acknowledgements

JZ was supported by the Division of Chemical Sciences, Geosciences and Biosciences, Office of Basic Energy Sciences, USDOE. Sandia National Laboratories is a multimission laboratory managed and operated by National Technology and Engineering Solutions of Sandia, LLC, a wholly owned subsidiary of Honeywell International, Inc., for USDOE's National Nuclear Security Administration under Contract DE-NA-0003525. ACD was supported by the U.S. Department of Energy, Office of Science, Office of Workforce Development for Teachers and Scientists, Office of Science Graduate Student Research (SCGSR) program. The SCGSR program is administered by the Oak Ridge Institute for Science and Education for the DOE under contract number DE-SC0014664. ACD was also supported by the National Science Foundation under Grant No. 2042646. BR thanks the support of [[JZ: add]] .

Notes and references

1 J. Zádor, C. A. Taatjes and R. Fernandes, *Progress in Energy and Combustion Science*, 2011, **37**, 371–421.

2 J. Zádor, H. Huang, O. Welz, J. Zetterberg, D. L. Osborn and C. A. Taatjes, *Physical Chemistry Chemical Physics*, 2013, **15**, 10753–10760.

3 J. D. Savee, E. Papajak, B. Rotavera, H. Huang, A. J. Eskola, O. Welz, L. Sheps, C. A. Taatjes, J. Zádor and D. L. Osborn, *Science*, 2015, **347**, 643–646.

4 A. S. Hansen, T. Bhagde, K. B. Moore, D. R. Moberg, A. W. Jasper, Y. Georgievskii, M. F. Vansco, S. J. Klippenstein and M. I. Lester, *Science*, 2021, **373**, 679–682.

5 A. S. Hansen, T. Bhagde, Y. Qian, A. Cavazos, R. M. Huchmala, M. A. Boyer, C. F. Gavin-Hanner, S. J. Klippenstein, A. B. McCoy and M. I. Lester, *The Journal of Chemical Physics*, 2021, **156**, 014301.

6 H. D. Alwe, M. P. Walavalkar, A. Sharma, S. Dhanya and P. D. Naik, *Atmospheric Environment*, 2014, **82**, 113–120.

7 S. Tang, L. Du, N. T. Tsona, H. Zhao and W. Wang, *Atmospheric Environment*, 2017, **162**, 23–30.

8 E. C. Minerath, M. P. Schultz and M. J. Elrod, *Environmental Science & Technology*, 2009, **43**, 8133–8139.

9 N. C. Cole-Filipiak, A. E. O'Connor and M. J. Elrod, *Environmental Science & Technology*, 2010, **44**, 6718–6723.

10 L. Vereecken and J. S. Francisco, *Chemical Society Reviews*, 2012, **41**, 6259–6293.

11 A. J. Kalafut-Pettibone, J. P. Klems, D. R. Burgess and W. S. McGivern, *The Journal of Physical Chemistry A*, 2013, **117**, 14141–14150.

12 S. M. Villano, L. K. Huynh, H. H. Carstensen and A. M. Dean, *J Phys Chem A*, 2012, **116**, 5068–89.

13 C. D. Wijaya, R. Sumathi and W. H. Green, *The Journal of Physical Chemistry A*, 2003, **107**, 4908–4920.

14 A. Miyoshi, *The Journal of Physical Chemistry A*, 2011, **115**, 3301–3325.

15 *Proceedings of the Combustion Institute*, 2017, **36**, 441–448.

16 M. Cord, B. Sirjean, R. Fournet, A. Tomlin, M. Ruiz-Lopez and F. Battin-Leclerc, *J Phys Chem A*, 2012, **116**, 6142–58.

17 M. G. Christianson, A. C. Doner, M. M. Davis, A. L. Koritzke, J. M. Turney, H. F. Schaefer, L. Sheps, D. L. Osborn, C. A. Taatjes and B. Rotavera, *International Journal of Chemical Kinetics*, 2021, **53**, 43–59.

18 A. C. Doner, M. M. Davis, A. L. Koritzke, M. G. Christianson, J. M. Turney, H. F. Schaefer III, L. Sheps, D. L. Osborn, C. A. Taatjes and B. Rotavera, *International Journal of Chemical Kinetics*, 2021, **53**, 127–145.

19 B. Rotavera and C. A. Taatjes, *Progress in Energy and Combustion Science*, 2021, **86**, 100925.

20 M. M. Davis, J. D. Weidman, A. S. Abbott, G. E. Douberly, J. M. Turney and H. F. SchaeferIII, *The Journal of Chemical Physics*, 2019, **151**, 124302.

21 G. Vanhove, Y. Yu, M. A. Boumehdi, O. Frottier, O. Herbinet, P.-A. Glaude and F. Battin-Leclerc, *Energy & Fuels*, 2015, **29**, 6118–6125.

22 A. J. Eskola, O. Welz, J. D. Savee, D. L. Osborn and C. A. Taatjes, *J Phys Chem A*, 2013, **117**, 12216–35.

23 Z. Serinyel, O. Herbinet, O. Frottier, P. Dirrenberger, V. Warth, P. A. Glaude and F. Battin-Leclerc, *Combust Flame*, 2013, **160**, 2319–2332.

24 E. J. Silke, W. J. Pitz, C. K. Westbrook and M. Ribaucour, *J Phys Chem A*, 2007, **111**, 3761–75.

25 S. M. Sarathy, T. Javed, F. Karsenty, A. Heufer, W. Wang, S. Park, A. Elwardany, A. Farooq, C. K. Westbrook, W. J. Pitz, M. A. Oehlschlaeger, G. Dayma, H. J. Curran and P. Dagaut, *Combustion and Flame*, 2014, **161**, 1444–1459.

26 Y. Sakai, J. Herzler, M. Werler, C. Schulz and M. Fikri, *Proceedings of the Combustion Institute*, 2017, **36**, 195–202.

27 C. Hemken, U. Burke, K. Y. Lam, D. F. Davidson, R. K. Hanson, K. A. Heufer and K. Kohse-Hoinghaus, *Combustion and Flame*, 2017, **184**, 195–207.

28 A. D. Danilack, C. R. Mulvihill, S. J. Klippenstein and C. F. Goldsmith, *The Journal of Physical Chemistry A*, 2021, **125**, 8064–8073.

29 O. Herbinet, F. Battin-Leclerc, S. Bax, H. Le Gall, P. A. Glaude, R. Fournet, Z. Zhou, L. Deng, H. Guo, M. Xie and F. Qi, *Phys Chem Chem Phys*, 2011, **13**, 296–308.

30 J. R. Duan, J. Ji, L. L. Ye, Y. T. Zhai and L. D. Zhang, *Proceedings of the Combustion Institute*, 2021, **38**, 681–689.

31 S. W. Hartness, N. S. Dewey, M. G. Christianson, A. L. Koritzke, A. C. Doner, A. R. Webb and B. Rotavera, *Proceedings of the Combustion Institute*, 2022, **39**, submitted.

32 R. Van de Vijver and J. Zádor, *Computer Physics Communications*, 2020, **248**, 106947.

33 I. O. Antonov, J. Zádor, B. Rotavera, E. Papajak, D. L. Osborn, C. A. Taatjes and L. Sheps, *The Journal of Physical Chemistry A*, 2016, **120**, 6582–6595.

34 B. Rotavera, J. D. Savee, I. O. Antonov, R. L. Caravan, L. Sheps, D. L. Osborn, J. Zádor and C. A. Taatjes, *Proceedings of the Combustion Institute*, 2017, **36**, 597–606.

35 M.-W. Chen, B. Rotavera, W. Chao, J. Zádor and C. A. Taatjes, *Physical Chemistry Chemical Physics*, 2018, **20**, 10815–10825.

36 2019, `https://github.com/zadorlab/KinBot`.

37 L. Sheps, A. L. Dewyer, M. Demireva and J. Zádor, *The Journal of Physical Chemistry A*, 2021, **125**, 4467–4479.

38 K. S. Lockwood and N. J. Labbe, *Proceedings of the Combustion Institute*, 2021, **38**, 533–541.

39 C. O. Rogers, K. S. Lockwood, Q. L. D. Nguyen and N. J. Labbe, *International Journal of Chemical Kinetics*, 2021, **53**, 1272–1284.

40 K. Ramasesha, J. D. Savee, J. Zádor and D. L. Osborn, *The Journal of Physical Chemistry A*, 2021, **125**, 9785–9801.

41 T. J. Lee and P. R. Taylor, *Int. J. Quant. Chem.*, 1989, **Supplement 23**, 199–207.

42 T. J. Lee, A. P. Rendell and P. R. Taylor, *J. Phys. Chem.*, 1990, **94**, 5463–5468.

43 E. Pollak and P. Pechukas, *Journal of the American Chemical Society*, 1978, **100**, 2984–2991.

44 M. K. Gilson and K. K. Irikura, *The Journal of Physical Chemistry B*, 2010, **114**, 16304–16317.

45 A. W. Jasper, *International Journal of Chemical Kinetics*, 2020, **52**, 387–402.

46 A. W. Jasper and J. A. Miller, *Combustion and Flame*, 2014, **161**, 101–110.

47 T. M. Lenhardt, C. E. McDade and K. D. Bayes, *Journal of Chemical Physics*, 1980, **72**, 304–310.

48 D. Wu and K. D. Bayes, *Int. J. Chem. Kinet.*, 1986, **18**, 547.

49 M. J. Frisch, G. W. Trucks, H. B. Schlegel, G. E. Scuseria, M. A. Robb, J. R. Cheeseman, G. Scalmani, V. Barone, G. A. Petersson, H. Nakatsuji, X. Li, M. Caricato, A. V. Marenich, J. Bloino, B. G. Janesko, R. Gomperts, B. Mennucci, H. P. Hratchian, J. V. Ortiz, A. F. Izmaylov, J. L. Sonnenberg, Williams, F. Ding, F. Lipparini, F. Egidi, J. Goings, B. Peng, A. Petrone, T. Henderson, D. Ranasinghe, V. G. Zakrzewski, J. Gao, N. Rega, G. Zheng, W. Liang, M. Hada, M. Ehara, K. Toyota, R. Fukuda, J. Hasegawa, M. Ishida, T. Nakajima, Y. Honda, O. Kitao, H. Nakai, T. Vreven, K. Throssell, J. A. Montgomery Jr., J. E. Peralta, F. Ogliaro, M. J. Bearpark, J. J. Heyd, E. N. Brothers, K. N. Kudin, V. N. Staroverov, T. A. Keith, R. Kobayashi, J. Normand, K. Raghavachari, A. P. Rendell, J. C. Burant, S. S. Iyengar, J. Tomasi, M. Cossi, J. M. Millam, M. Klene, C. Adamo, R. Cammi, J. W. Ochterski, R. L. Martin, K. Morokuma, O. Farkas, J. B. Foresman and D. J. Fox, *Gaussian 16 Rev. B.01*, 2016.

50 H. J. Werner, P. J. Knowles, G. Knizia, F. R. Manby and M. Schutz, *Wiley Interdisciplinary Reviews-Computational Molecular Science*, 2012, **2**, 242–253.

51 H.-J. Werner, P. J. Knowles, F. R. Manby, J. A. Black, K. Doll, A. Heßelmann, D. Kats, A. Köhn, T. Korona, D. A. Kreplin, Q. Ma, T. F. Miller, A. Mitrushchenkov, K. A. Peterson, I. Polyak, G. Rauhut and M. Sibaev, *The Journal of Chemical Physics*, 2020, **152**, 144107.

52 H.-J. Werner, P. J. Knowles, G. Knizia, F. R. Manby, M. Schütz, P. Celani, W. Györffy, D. Kats, T. Korona, R. Lindh, A. Mitrushenkov, G. Rauhut, K. R. Shamasundar, T. B. Adler, R. D. Amos, S. J. Bennie, A. Bernhardsson, A. Berning, D. L. Cooper, M. J. O. Deegan, A. J. Dobbyn, F. Eckert, E. Goll, C. Hampel, A. Hesselmann, G. Hetzer, T. Hrenar, G. Jansen, C. Köppl, S. J. R. Lee, Y. Liu, A. W. Lloyd, Q. Ma, R. A. Mata, A. J. May, S. J. McNicholas, W. Meyer, T. F. Miller III, M. E. Mura, A. Nicklass, D. P. O'Neill, P. Palmieri, D. Peng, K. Pflüger, R. Pitzer, M. Reiher, T. Shiozaki, H. Stoll, A. J. Stone, R. Tarroni, T. Thorsteinsson, M. Wang and M. Welborn, *MOLPRO, version 2020.1, a package of ab initio programs*, see.

53 *Atomic Simulation Environment*, `https://wiki.fysik.dtu.dk/ase/`.

54 R. Van de Vijver, *PESViewer*, 2018, `https://github.com/rubenvdvijver/PESViewer`.

55 Y. Georgievskii, J. A. Miller, M. P. Burke and S. J. Klippenstein, *Journal of Physical Chemistry A*, 2013, **117**, 12146–54.

56 Y. Georgievskii and S. J. Klippenstein, *MESS.2016.3.23.*

57 M. G. Christianson, A. C. Doner, M. M. Davis, A. L. Koritzke, J. M. Turney, H. F. Schaefer III, L. Sheps, D. L. Osborn, C. A. Taatjes and B. Rotavera, *International Journal of Chemical Kinetics*, 2021, **53**, 43–59.

58 N. J. DeYonker, T. R. Cundari and A. K. Wilson, *The Journal of Chemical Physics*, 2006, **124**, 114104.

59 A. M. Scheer, O. Welz, D. Y. Sasaki, D. L. Osborn and C. A. Taatjes, *Journal of the American Chemical Society*, 2013, **135**, 14256–14265.

60 J. Bugler, B. Marks, O. Mathieu, R. Archuleta, A. Camou, C. Grégoire, K. A. Heufer, E. L. Petersen and H. J. Curran, *Combustion and Flame*, 2016, **163**, 138–156.

61 M. Berasategui, D. Amedro, L. Vereecken, J. Lelieveld and J. N. Crowley, *Atmospheric Chemistry and Physics*, 2020, **20**, 13541–13555.

62 J. D. Crounse, K. A. McKinney, A. J. Kwan and P. O. Wennberg, *Analytical Chemistry*, 2006, **78**, 6726–6732.

63 M. Fels and W. Junkermann, *Geophysical Research Letters*, 1994, **21**, 341–344.

64 S. Z. He, Z. M. Chen, X. Zhang, Y. Zhao, D. M. Huang, J. N. Zhao, T. Zhu, M. Hu and L. M. Zeng, *Journal of Geophysical Research: Atmospheres*, 2010, **115**,.

65 X. Zhang, Z. M. Chen, S. Z. He, W. Hua, Y. Zhao and J. L. Li, *Atmospheric Chemistry and Physics*, 2010, **10**, 737–748.

66 K. A. Sahetchian, R. Rigny, J. Tardieu de Maleissye, L. Batt, M. Anwar Khan and S. Mathews, *Symposium (International) on Combustion*, 1992, **24**, 637–643.

67 J. Zádor, R. X. Fernandes, Y. Georgievskii, G. Meloni, C. A. Taatjes and J. A. Miller, *Proc. Combust. Inst.*, 2009, **32**, 271–277.

68 M. P. Rissanen, D. Amedro, A. J. Eskola, T. Kurten and R. S. Timonen, *The Journal of Physical Chemistry A*, 2012, **116**, 3969–3978.

69 J. A. Miller, R. Sivaramakrishnan, Y. Tao, C. F. Goldsmith, M. P. Burke, A. W. Jasper, N. Hansen, N. J. Labbe, P. Glarborg and J. Zádor, *Progress in Energy and Combustion Science*, 2021, **83**, 100886.

70 J. A. Miller, S. J. Klippenstein, S. H. Robertson, M. J. Pilling, R. Shannon, J. Zádor, A. W. Jasper, C. F. Goldsmith and M. P. Burke, *Journal of Physical Chemistry A*, 2016, **120**, 306–312.